

10

Time projection chambers

10.1 Introduction: the precursors

Various designs of drift chamber, with large sensitive gas volumes coupled to planes of multiplying wires, have been described in the previous chapter. As the event separation depends on the maximum drift time, or memory, of the detector, in many applications the drift volume thickness is kept relatively small. For low event rates, or for use at storage ring accelerators where the collision frequency is low, long drift lengths can be used; providing a full three-dimensional representation of events, large volume drift chambers have also been named imaging chambers. While this implies a strict control on gas purity and requires high voltage values, it considerably reduces the complexity of the readout device and electronics.

An early example of very large volume, single-ended readout drift chamber is the detector built for the identification of secondary particles by ionization sampling (ISIS and ISIS2), operated at CERN in the mid-1970s (Allison *et al.*, 1974) and consisting of a large gas box with field-shaping electrodes on the walls, between two cathodes and a central wire plane for amplification and detection of ionization trails, shown in Figure 10.1 (Allison *et al.*, 1984). Drift time and signal charge are recorded on each anode wire, providing the vertical coordinate and the charge for the corresponding track segments, the second coordinate is given by the anode wire number. Figure 10.2 is an example of a multi-track single event recorded in a beam exposure with ISIS2; the vertical scale corresponds to the two metre drift volume length. The device was used as part of the European Hybrid Spectrometer, providing both the particles' trajectory and the differential energy loss used for particle identification in the low momentum region.

Due to its conception, the ISIS device can be considered as a precursor of the time projection chamber, to be described in the following sections.



Figure 10.1 The large volume ISIS2 chamber (Allison *et al.*, 1984). By kind permission of Elsevier.

10.2 Principles of operation

Knowledgeable of the successful development of large volume drift chambers and of the coordinate localization method from cathode induced signals in MWPCs, David Nygren and collaborators proposed in 1976 a new detector concept named the time projection chamber (TPC) for the PEP-4 experimental area at SLAC (Clark *et al.*, 1976; Nygren and Marx, 1978; Aihara *et al.*, 1983).

In its basic design, the TPC consists of a large volume of gas with field shaping electrodes, terminating at one end with a multi-wire end-cap chamber plane having alternating anode and field wires; the two parts are separated by a cathode mesh permitting one to set the drift and multiplication field independently. On the outer side of the MWPC, the cathode plane consists of a printed circuit board with pad rows parallel to the anodes, shown schematically in Figure 10.3. Electrons released by ionization trails in the main volume drift towards the end-cap, cross the first

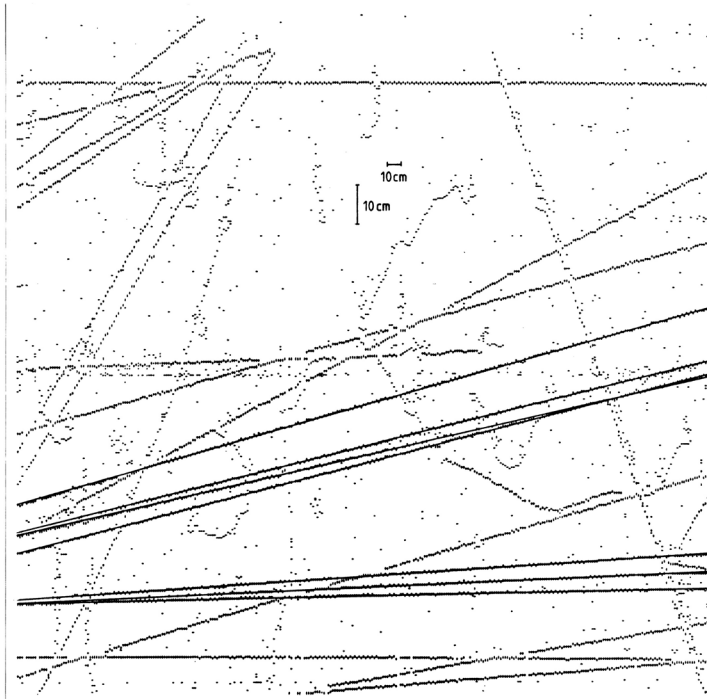


Figure 10.2 An event recorded with the ISIS drift chamber (Allison *et al.*, 1984). By kind permission of Elsevier.

mesh electrode, and are collected and amplified on the anode wires, thus producing a negative signal on the anodes and a positive charge induction profile on the corresponding pad rows, as shown schematically in Figure 10.4. A recording of the charge distribution on the pads in successive time slices provides the drift time and longitudinal coordinate of track segments, as well as the differential ionization energy loss; signals on wires can be also recorded to improve the drift time measurement.

In most TPC applications, the major information is the one projected on the MWPC plane, or azimuthal, provided by the pad rows, and therefore a large effort has been devoted to measurements and simulations of the induced signal distribution, the so-called pad response function, determining the localization properties of the detector. Operation in a strong magnetic field parallel to the drift field, with an appropriate choice of the gas filling, reduces the transverse diffusion and hence its contribution to the dispersion of the collected charge for long drift distances, with an ensuing improvement in localization accuracy as discussed in Chapter 4. Figure 10.5 (Clark *et al.*, 1976) shows the estimated reduction of diffusion for several common gases; while well known to gaseous electronics experts, this property, basic for the TPC operation, was not familiar at the time to the gas detector community.

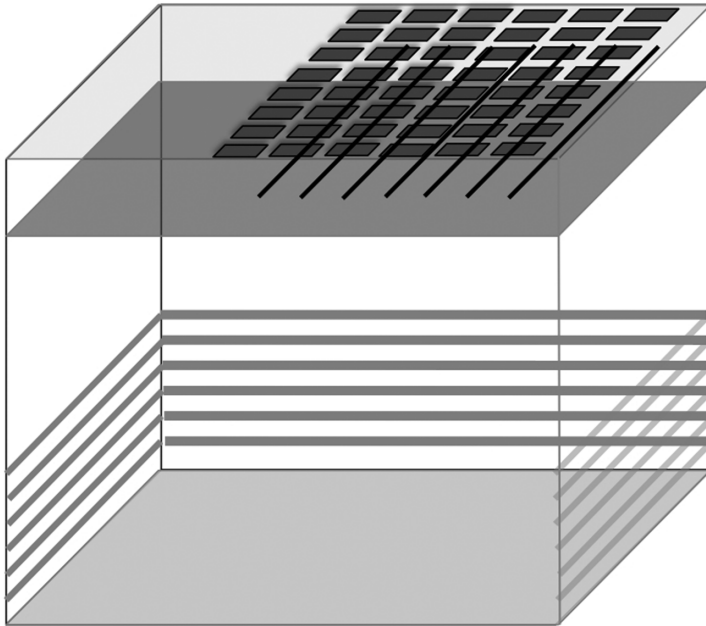


Figure 10.3 Schematics of a time projection chamber: ionizing trails produced in a large volume of gas drift to an end-cap MWPC with cathode pad rows.

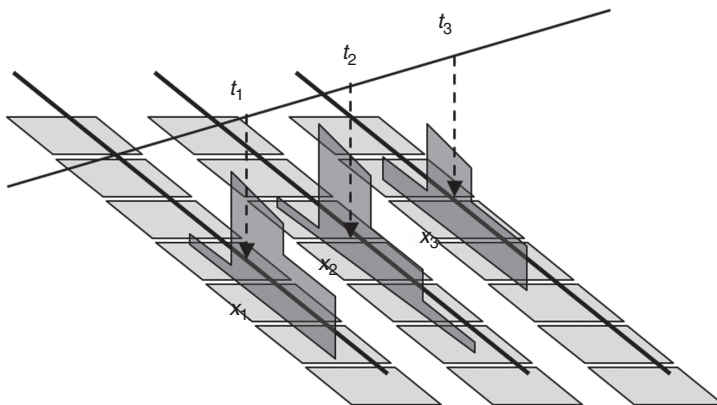


Figure 10.4 The charge induction process on the pad rows.

Adapted for operation in a solenoidal magnet, the PEP-4 TPC, as well as many similar devices implemented later, had the cylindrical shape shown schematically in Figure 10.6 (redrawn from Clark *et al.*, 1976), with two independent, back-to-back detectors having a common central high-voltage drift electrode, and two composite MWPC end-caps for amplification and signal recording (Figure 10.7). To optimize the particle identification power and momentum resolution, the PEP-4

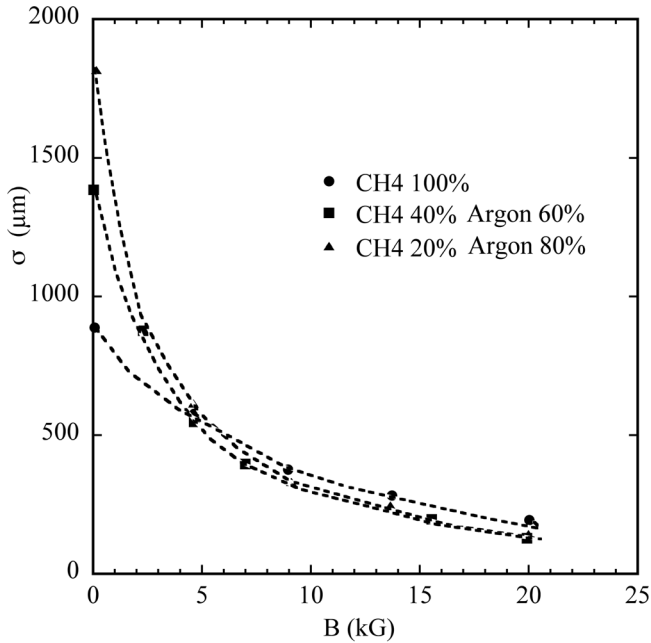


Figure 10.5 Dependence of the transverse electron diffusion on magnetic field for several gas mixtures. Data from Clark *et al.* (1976).

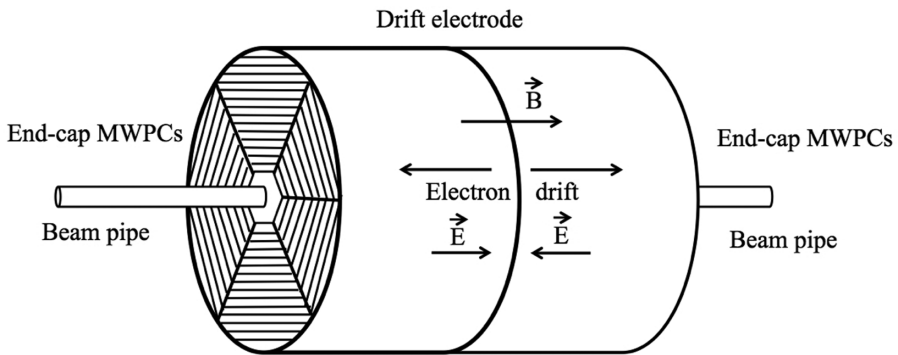


Figure 10.6 Schematics of the PEP-4 TPC.

TPC was operated at high pressures (argon–methane at 8.5 bars); for practical and security reasons, most of the later TPC systems have been operated at pressures close to atmospheric.

An example of a multi-prong event recorded with the PEP-4 TPC is shown in Figure 10.8; represented as three independent projections, the information is in fact fully three-dimensional. The particle identification power of the device, deduced from a weighted average of the 185 independent differential energy loss measurements for each track, is seen in Figure 10.9 (Nygren, personal communication).

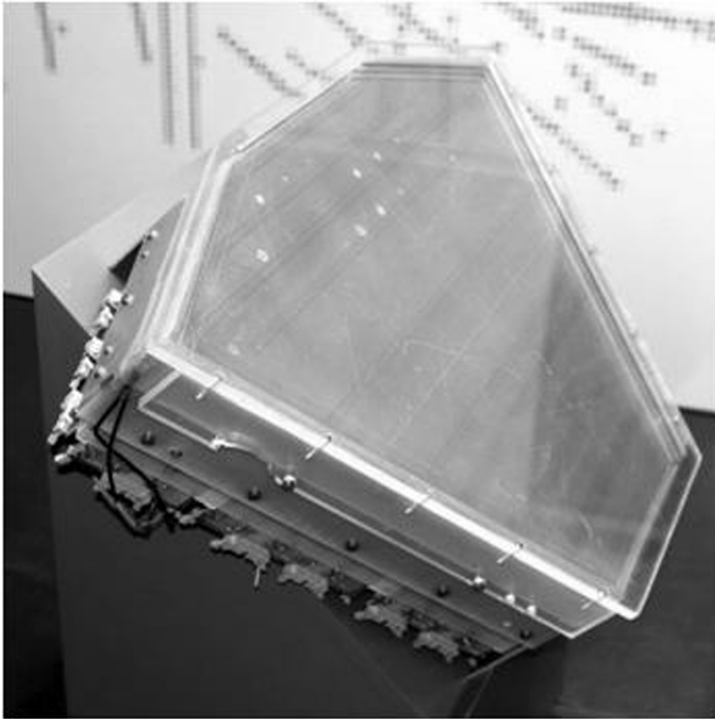


Figure 10.7 One of the MWPC modules for the LBL PEP-4 TPC. D. Nygren, personal communication (1985).

10.3 TPC-based experiments

Time projection chambers have been built and successfully operated in many colliding beam and fixed target experiments, demonstrating excellent imaging and particle identification capabilities, particularly for large track multiplicities. Due to the long memory time, several tens of microseconds or more, TPCs find their natural use for electron–positron storage rings having comparable collision frequencies, as the now discontinued LEP at CERN and TRISTAN at KEK, low rate fixed target experiments as TRIUMF in Vancouver, very high multiplicity heavy ions collisions as NA49 at CERN and STAR at RHIC, and the gigantic ALICE TPC at CERN. Smaller devices are used in many other experiments both in high-energy and nuclear physics; cryogenic TPCs, making use of liquid noble gases, are also under development and are described in Chapter 15. For summaries of the early developments, see, for example, the proceedings of the Time Projection Chamber Conference (TPC (1983)) and the book of Blum and Rolandi (1993).

Figure 10.10 is a perspective view of the TRIUMF TPC, one of the first devices of this kind to be operated after the original PEP4 development, and used for the study of muon decays (Hargrove *et al.*, 1984). The quoted reference includes also

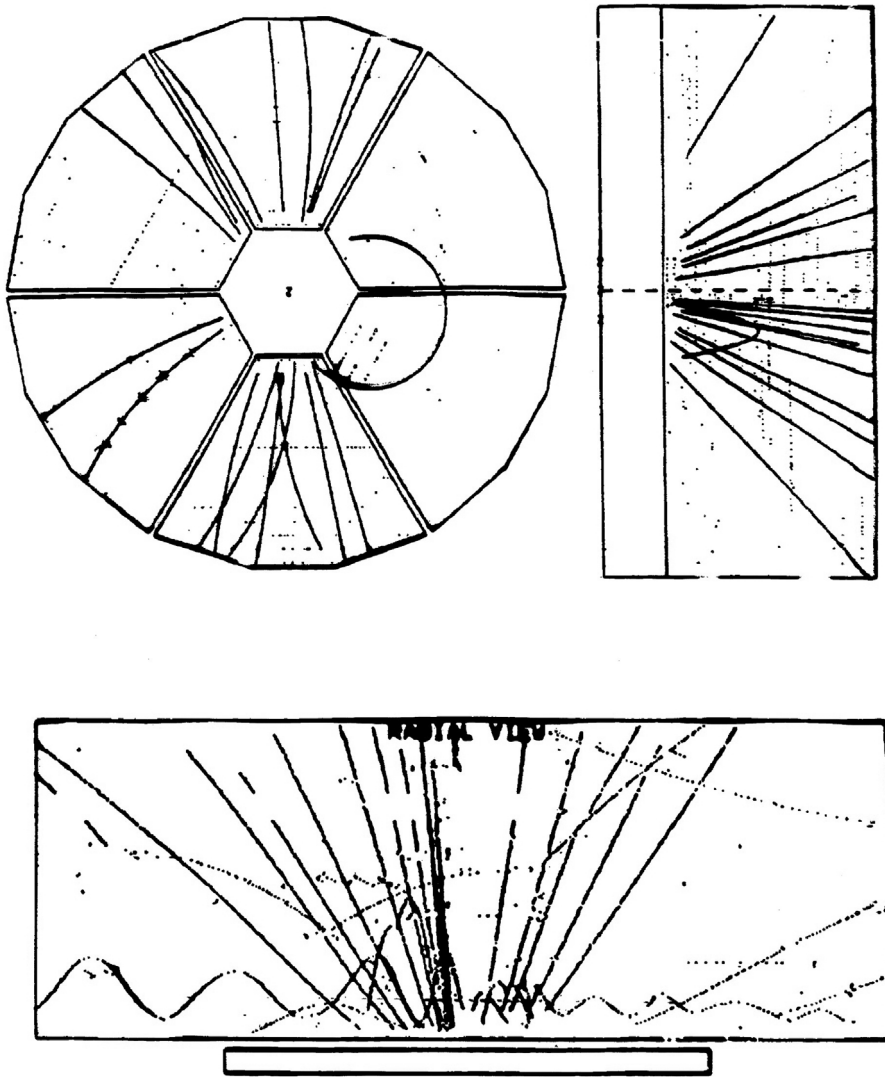


Figure 10.8 Projection on three planes of an event recorded with the PEP-4 TPC
D. Nygren, personal communication (1985).

one of the first detailed studies of the effects of magnetic field and track angle on resolution (see the next section).

Figure 10.11 shows the schematics of the ALEPH TPC, operated at LEP from its commissioning in 1989 to the end of operation of the collider in December 2000, and the picture in Figure 10.12 is a front view of the full detector with the TPC end-cap system recognizable from the composite shape of the MWPCs used for the readout (Decamp *et al.*, 1990); Figure 10.13 is an example of on-line event

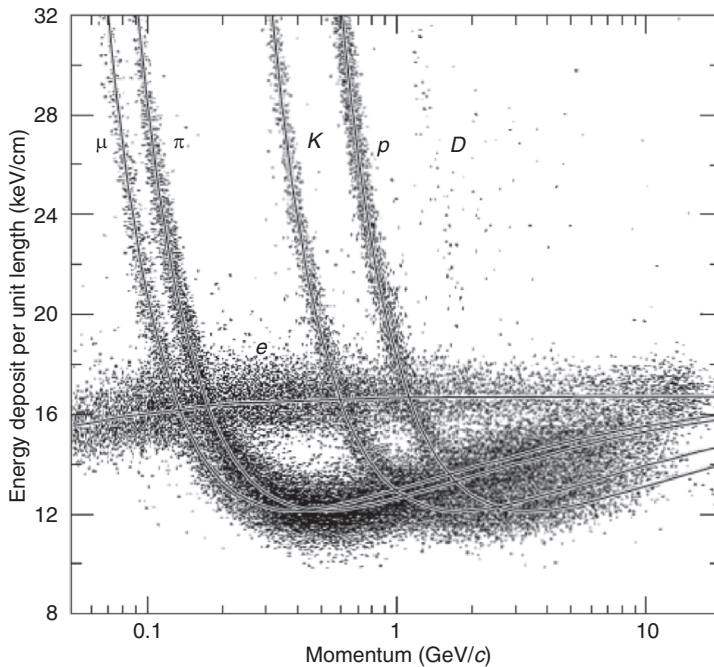


Figure 10.9 Particle identification power of the PEP-4 TPC, operated at 8.5 bars. The momentum is given by the tracks' curvature in the 0.4 T magnetic field. D. Nygren, personal communication (1985).

display for the device. Similar in conception and performances, the DELPHI TPC equipped a second collision point at LEP (Brand *et al.*, 1989).

The design of the cylindrical double back-to-back TPC, with the composite field cage and the MWPC sensors arrays at the two outer ends, has become, with small variations, a standard for detectors inserted in a solenoidal magnets around storage rings. Figure 10.14 shows the field cage and end-cap support structure of the STAR TPC at Brookhaven's RHIC heavy ions collider (STAR), and Figure 10.15 the projection on the end-cap plane of a heavily populated multi-track event in a gold–gold collision at 30+30 GeV (Anderson *et al.*, 2003). Two smaller devices with radial drift geometry, named forward TPCs, complement the main system to extend detection at lower angles to the beam axis (Ackermann *et al.*, 2003).

With an outer diameter close to 5 metres and active volume around 100 m³, the ALICE TPC installed at CERN's LHC is the largest device of this kind ever built, Figure 10.16 and Figure 10.17 (Alme *et al.*, 2010); the picture in Figure 10.18 shows Peter Glässel, the TPC technical coordinator, sitting within the central opening of the end-cap array. Used for the detection of heavy ion collisions, the device is capable of reconstructing very complex events; Figure 10.19 is an example of outcomes of a lead–lead collision at 2.76 TeV. The detector also performs

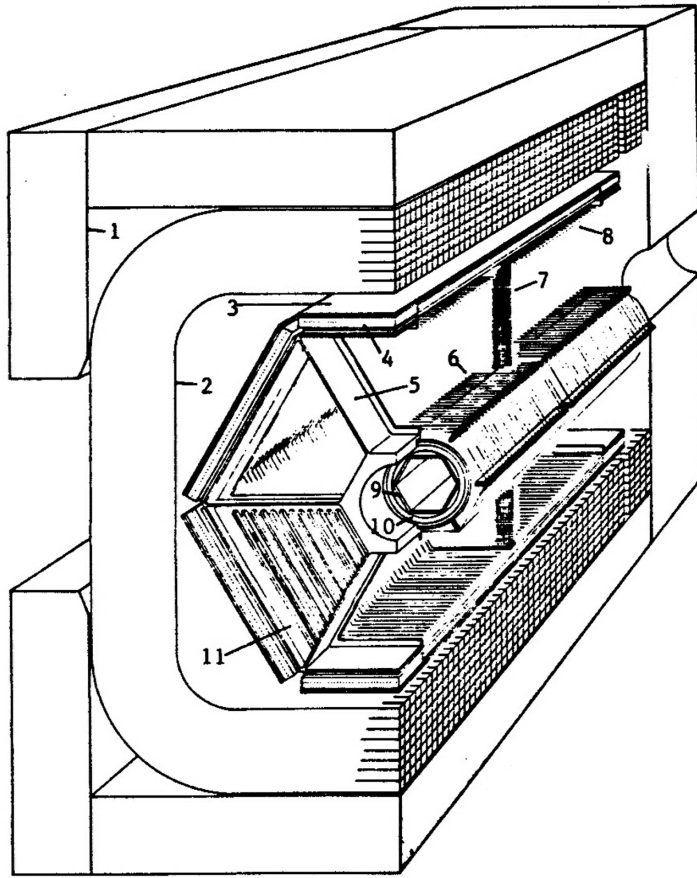


Figure 10.10 Perspective cut view of the TRIUMF TPC (Hargrove *et al.*, 1984).
By kind permission of Elsevier.

particle identification, particularly in the low momentum range, from the analysis of the recorded differential energy loss of the tracks, Figure 10.20 (You, 2012).

A simpler, box-like TPC design is used for fixed target experiments. The NA49 large acceptance detector includes along the interacting beam line a pair of medium-size vertex TPCs and two larger main TPCs to detect the interaction yields; Figure 10.21 shows a view inside the main TPC field cage; Figure 10.22 is a reconstructed event resulting from a high-energy lead–lead interaction.

While in the current generation of TPCs the end-cap detector is implemented with multi-wire chamber modules, the recent developments of micro-pattern gas detectors have suggested the use of these devices to improve performances, and in particular the localization accuracy and multi-track resolution (Kappler *et al.*, 2004; Ableev *et al.*, 2004; Radicioni, 2007). A medium-size TPC with

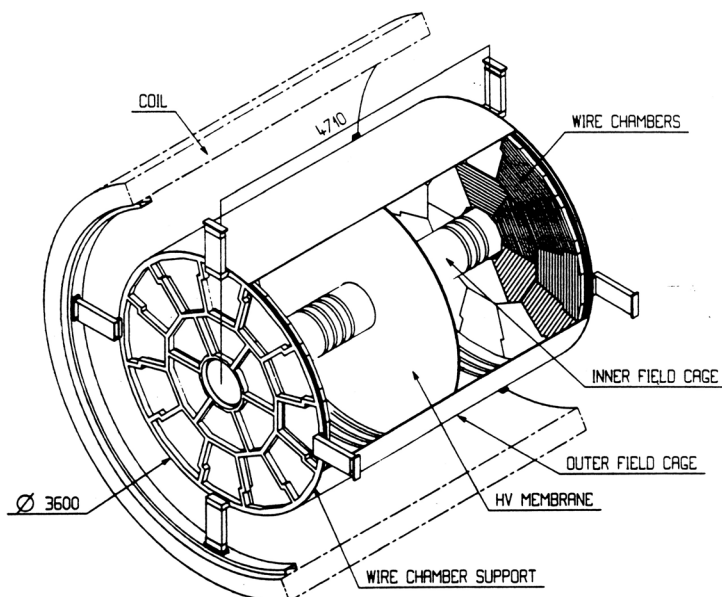


Figure 10.11 Artist's view of the ALEPH TPC assembly (Decamp *et al.*, 1990).
By kind permission of Elsevier.

Micromegas readout is already operational in the experiment T2K (Abgrall *et al.*, 2011) and both Micromegas and GEM-based readouts are investigated for the large TPC under development for the International Linear Collider (ILC) (Behnke, 2011) and the ALICE GEM-TPC upgrade (Böhmer *et al.*, 2013). Performances of these devices are discussed in Chapter 13.

10.4 Signal induction: the pad response function

As shown schematically in Figure 10.4, the multiplication process occurring on the anodes when the ionization trail reaches the wires results in the appearance on the facing pad rows of an induced charge profile around the position of the avalanches. The profile evolves with time, reaching a maximum in front of the avalanches at the time of full collection of the corresponding segment of primary ionization. The screening effect of the field wires and the separation between pad rows minimizes cross-talk problems.

As discussed in Sections 6.3 and 8.9, for a point-like avalanche the charge induction profile on the cathode plane has a two-dimensional Gaussian-like shape, building up and then decreasing with time, with a FWHM approximately equal to twice the anode-to-cathode distance, or gap G . Recording and suitable analysis of

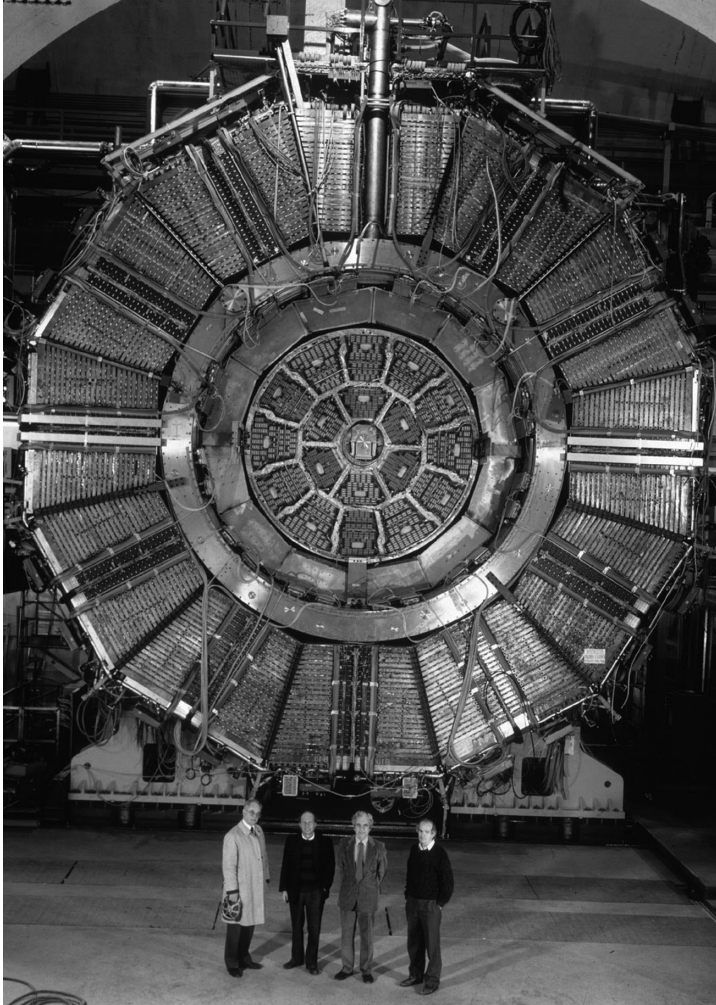


Figure 10.12 Open-ended front view of the ALEPH detector. The spokesman of the experiment and Nobel Laureate Jack Steinberger stands third from left. Picture CERN (1988).

the charge induction profile on pads or strips provides the coordinate of the avalanche along the anode wire.

Projected in the direction x parallel to the anode wire, the distribution is approximated by the expression (see Figure 10.23 for the definition of parameters):

$$P(x) \approx e^{-\frac{x^2}{2\sigma^2}}, \quad \sigma = \frac{2G}{2.34}. \quad (10.1)$$

Integration over the area of the strip provides the so-called intrinsic pad response function (PRF), describing the dependence of the induced signal on the pad

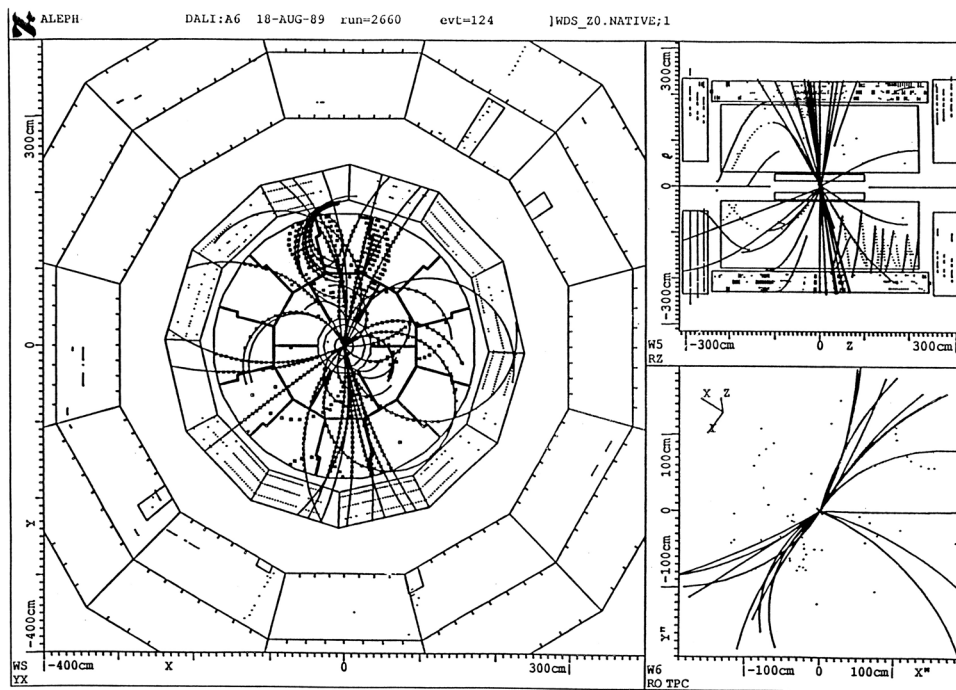


Figure 10.13 On-line display of an event recorded with the ALEPH TPC. Picture CERN (1991).

geometry and position with respect to the avalanche; for the simple case of a track parallel to the strip it can be written as (Blum and Rolandi, 1993):

$$P_0(X) = \int_{X-W/2}^{X+W/2} P(x)dx, \tag{10.2}$$

where W is the pad width and X the distance between the track and the centre of the pad. An example of the agreement between computed and measured distributions for a 4 mm gap chamber with 7 mm pads is shown in Figure 10.24 (Hargrove *et al.*, 1984).

While a small pad size W provides more measurements, thus improving localization, sharing of the charge reduces the ratio signal over noise; for best performances, a good choice is a pad width close to the gap size, $W \approx G$, for which most of the induced charge is shared between three adjacent pads. In this case, a simple algorithm can be used to compute the coordinate and the Gaussian width of the avalanches along the wire from the measured charges on three adjacent pads, Q_1 , Q_2 and Q_3 (Anderson *et al.*, 2003):



Figure 10.14 Field cage support structure of the STAR TPC at RHIC. Picture courtesy Brookhaven National Laboratory (USA).

$$X = \frac{\sigma^2}{2W} \ln\left(\frac{Q_3}{Q_1}\right), \quad \sigma^2 = \frac{W^2}{\ln(Q_2^2/Q_1Q_3)}, \quad (10.3)$$

where one should note that the charge on the central pad does not affect the coordinate measurement. The pad length L does not appear in the expressions, but determines the total value of the induced charge and affects the coordinate localization for inclined tracks and in the presence of a magnetic field, as discussed later.

In the real case of detection of the extended ionization trails released by charged particles, the electrons reaching the anode are not point-like, but spread along the wire depending on the geometry of the track and detector. For a proper description of the cathode-induced signals and the position resolution limits, the following effects have to be taken into account:

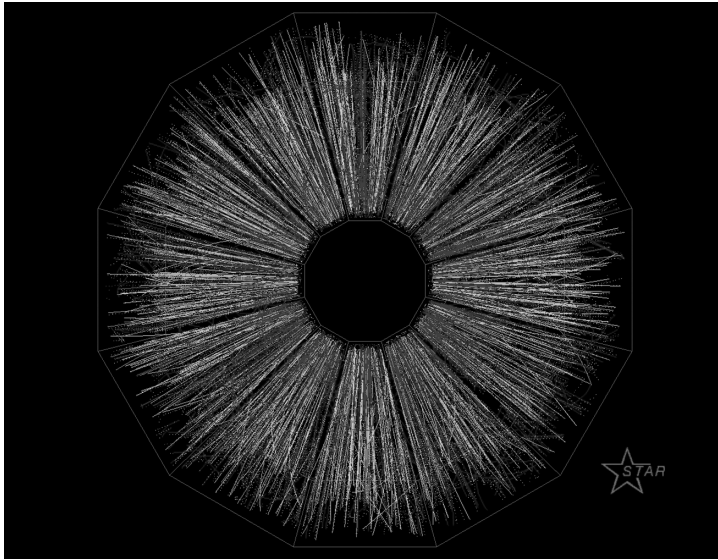


Figure 10.15 A gold–gold collision recorded with the STAR TPC (STAR). Picture courtesy Brookhaven National Laboratory (USA).

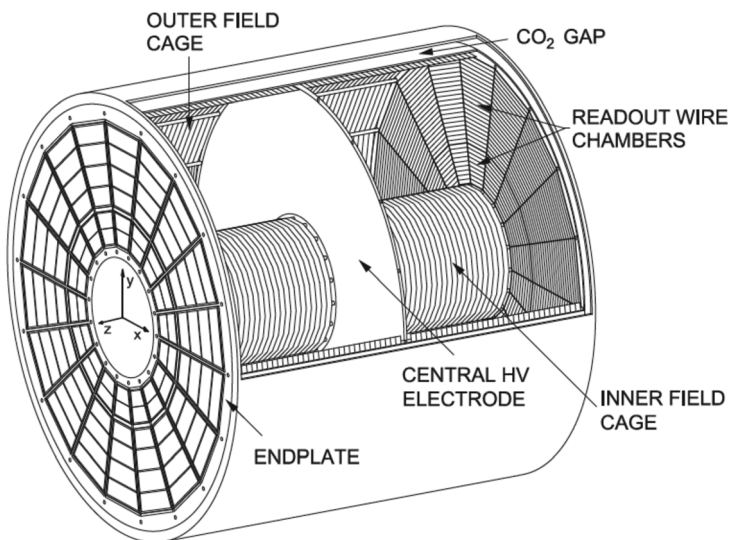


Figure 10.16 Artist's view of the ALICE TPC (Alme *et al.*, 2010). By kind permission of Elsevier.

- diffusion of electrons in their drift to the end-cap detector;
- spread due to the angle of the tracks with respect to the anode wire;
- distortions in the drift path when electrons approach the anode in the presence of a magnetic field, the so-called $E \times B$ effect;
- asymmetry in the energy loss distribution due to clusters.



Figure 10.17 A segment of the ALICE TPC MWPC end-cap. Picture CERN (2002).

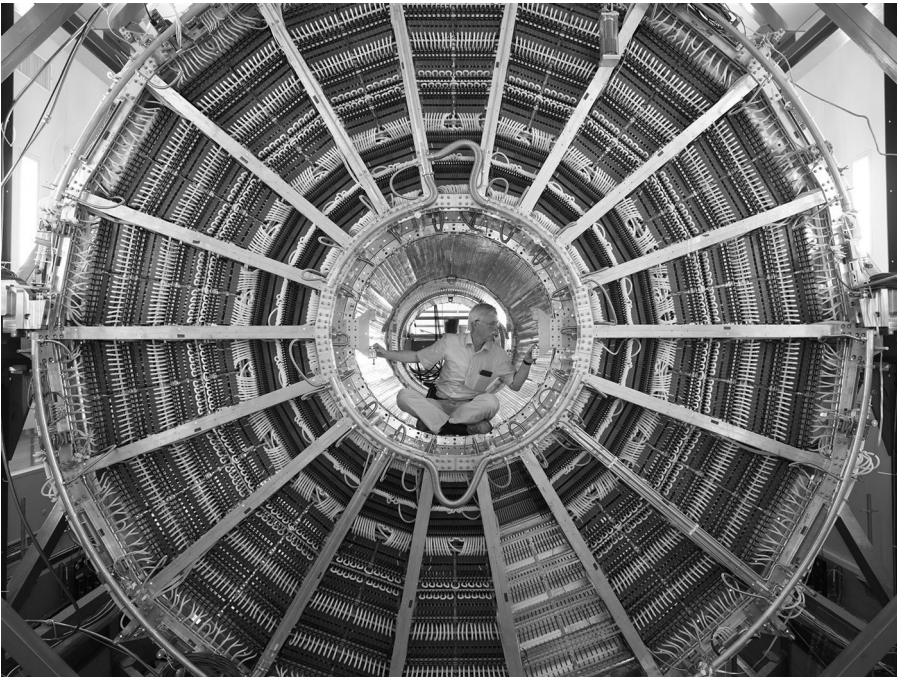


Figure 10.18 Front view of the ALICE TPC end-plate, with the technical coordinator, Peter Glassel. Picture CERN (2006).

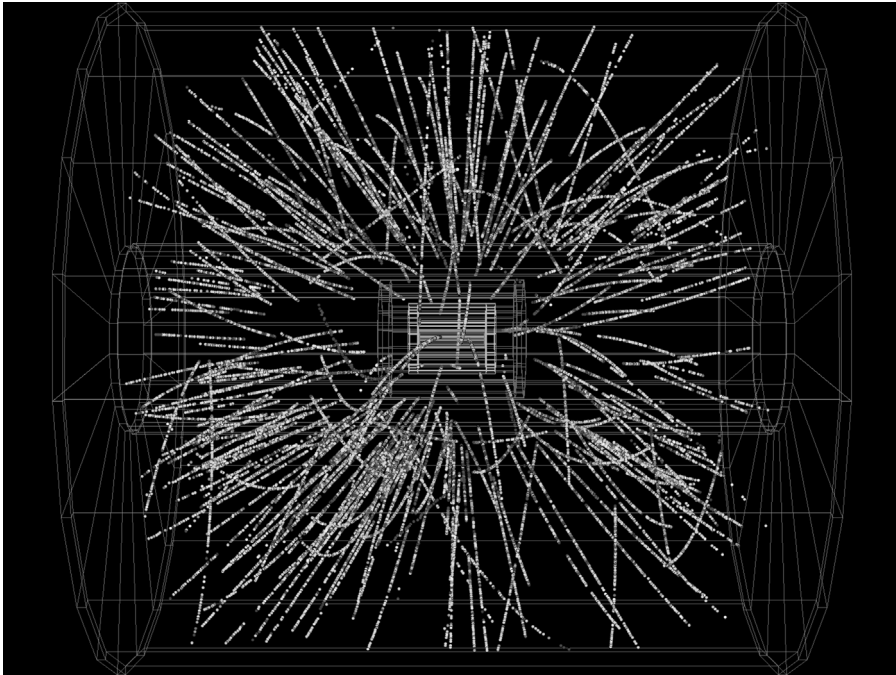


Figure 10.19 A proton–lead interaction recorded with the ALICE TPC at LHC. Picture CERN (2012).

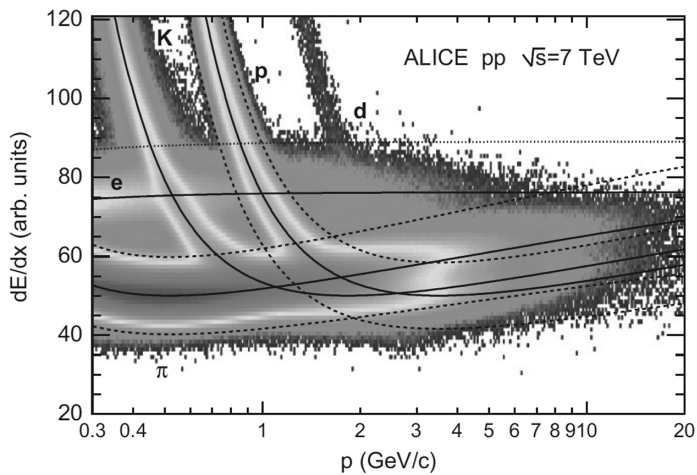


Figure 10.20 Particle identification with the ALICE TPC (You, 2012). By kind permission of Elsevier.



Figure 10.21 Inner view of one of the NA49 TPC modules. Picture CERN (1994).

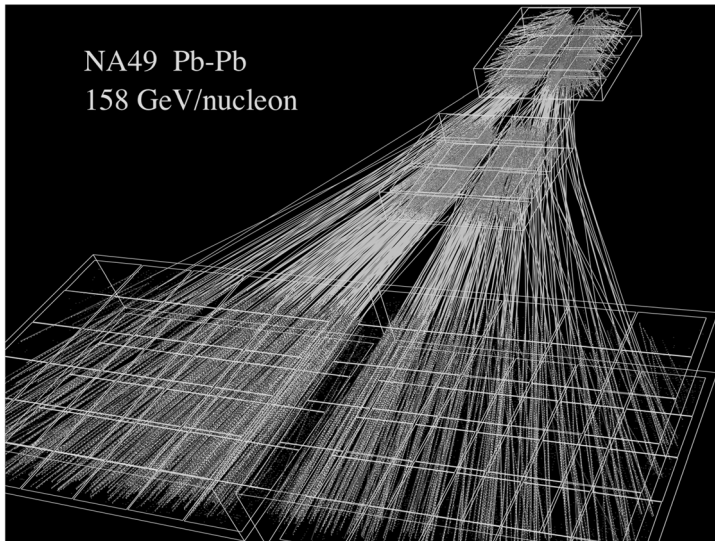


Figure 10.22 A lead–lead interaction recorded with the NA49 TPC complex. Picture CERN (1996).

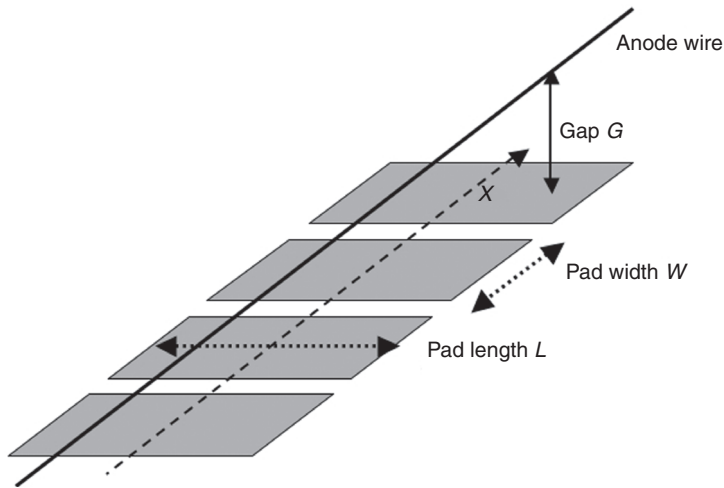


Figure 10.23 Schematics and definitions of the pad row geometry.

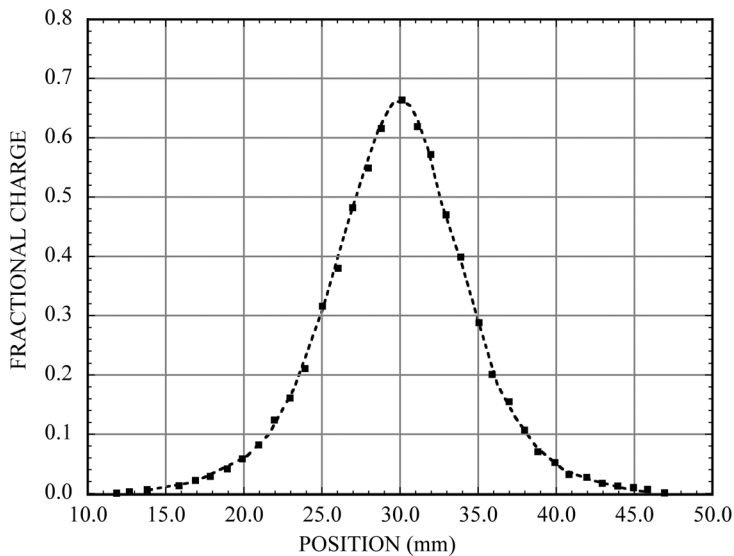


Figure 10.24 Measured (dots) and computed pad response function (curve) (Hargrove *et al.*, 1984). By kind permission of Elsevier.

Many authors have analysed the various dispersive effects and their consequences on the localization properties of the detector (Hargrove *et al.*, 1984; Blum *et al.*, 1986; Amendolia *et al.*, 1989; Saquin, 1992; Anderson *et al.*, 2003); an exhaustive discussion on the subject can be found in the textbook by Blum and Rolandi (1993).

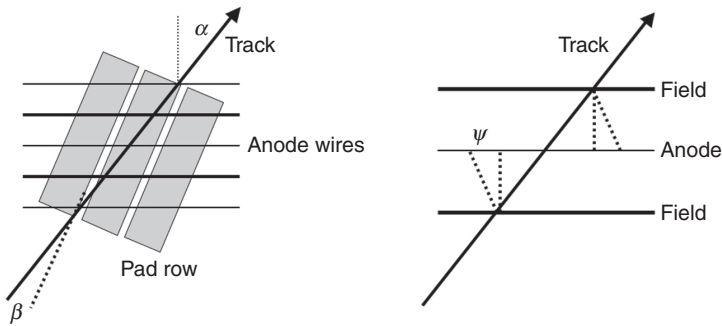


Figure 10.25 Angles between the track, wires and pads (left), and the deflection angle in a magnetic field (right).

The TPC space resolution in the direction of the anodes can be written as the squared sum of four independent contributions (Saquin, 1992):

$$\sigma^2 = \sigma_0^2 + \sigma_D^2(1 + \tan^2 \alpha) \cos^2(\alpha - \beta)L + \sigma_A^2(\tan \alpha - \tan \psi)^2 \cos^2(\alpha - \beta) + \sigma_P^2 \tan^2 \beta; \quad (10.4)$$

the dispersive terms in the sum correspond, respectively, to the point-like PRF, the electron diffusion over the drift length L , the magnetic deflection due to the $E \times B$ effect, and to the angle of the tracks. The quantities α , β are the angles of the track with the normal to the anodes and to the pad row direction and ψ is the angle due to the $E \times B$ effect (Figure 10.25); σ_D , σ_A and σ_P are ad-hoc constants corresponding to the respective dispersive effects. For the special case of a pad row parallel to the anodes, the expression simplifies as:

$$\sigma^2 = \sigma_0^2 + \sigma_D^2(1 + \tan^2 \alpha)L + \sigma_A^2(\tan \alpha - \tan \psi)^2. \quad (10.5)$$

The various constants appearing in the expressions can be deduced from simulations, or from a fit to measured data. As examples, Figure 10.26 and Figure 10.27 show the dependence of the azimuthal resolution on the drift length L and pad crossing angle β , the second and fourth terms in expression (10.4), measured with the ALEPH TPC at 1.5 T (Atwood *et al.* 1991).

The combined effects of geometry and magnetic deflection angle (third term in the expression) are seen in the example of Figure 10.28 measured with the DELPHI TPC (Brand *et al.*, 1986). As a consequence of the $E \times B$ distortion, the minimum is observed for tracks crossing the detector at an angle corresponding to the average deflection of the ionized trail due to the Lorentz force. In the absence of a magnetic field, the best localization accuracy is obtained for tracks perpendicular to the anodes, minimizing the angular dispersion factors.

In the previous considerations, the ionization density along the track was considered uniform. As discussed in Section 2.4, the presence of asymmetries in

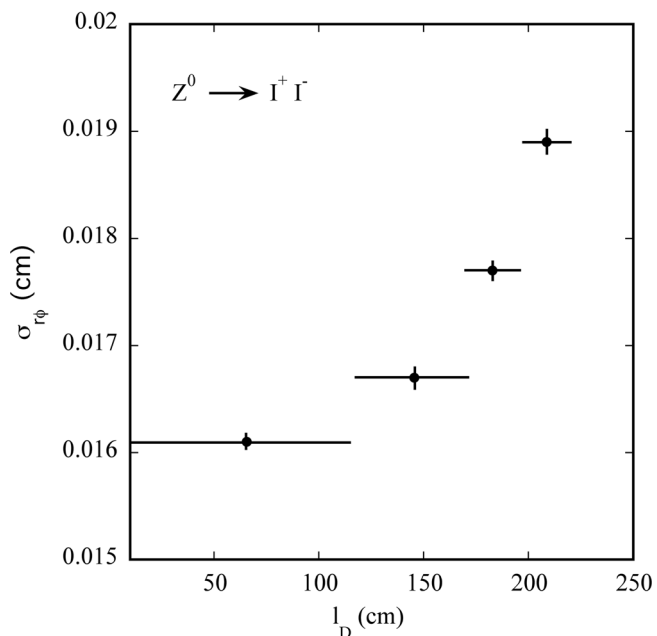


Figure 10.26 Dependence of the azimuthal localization accuracy on the drift length (Atwood *et al.*, 1991). By kind permission of Elsevier.

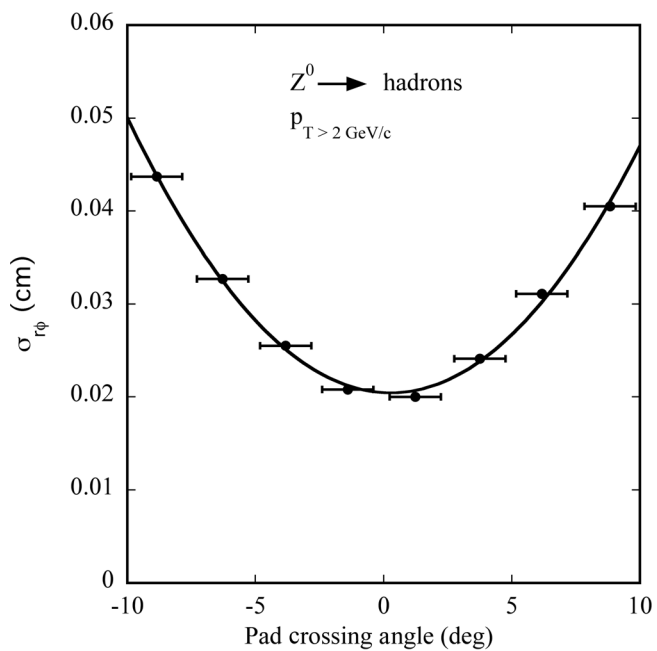


Figure 10.27 Dependence of the localization accuracy on the angle between tracks and pad row (Atwood *et al.*, 1991). By kind permission of Elsevier.

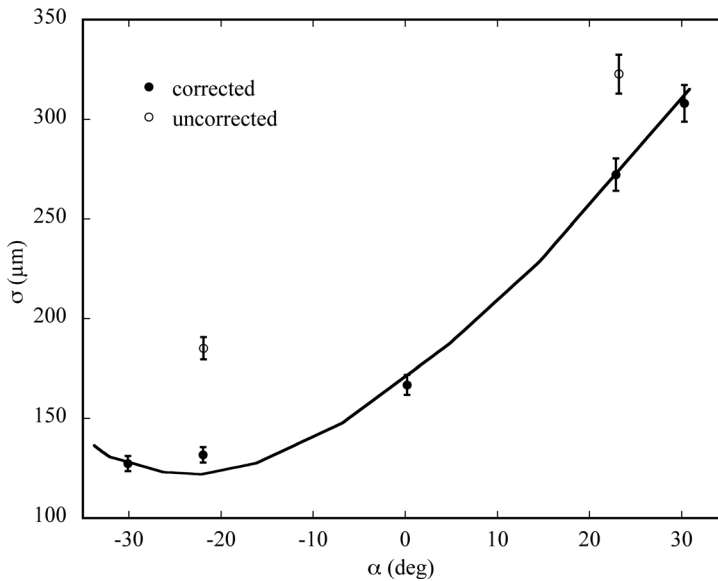


Figure 10.28 TPC position accuracy as a function of the track angle, measured at 1.2 T (Brand *et al.*, 1986). By kind permission of Elsevier.

the energy loss due to delta electrons (clusters) contributes to the worsening of the space resolution. Interestingly, for long drift paths, electron diffusion smears the trails, resulting in a more uniform charge distribution, an effect named declustering; the effect tends to improve the position accuracy for large angles and drift lengths, and has been studied with dedicated Monte Carlo simulations taking into account the energy loss and drift properties (Blum *et al.*, 1986). Figure 10.29 is an example of computed dependence of the position accuracy from the track's angle and several values of the drift length at 1.5 T; points with error bars are experimental values (Sharma, 1996). Owing to the declustering effect, at large angles the resolution is better for a long drift.

As seen from expression (10.4), the best projected localization accuracy is obtained for a track perpendicular to the pad rows. For large end-cap MWPC modules, radial rows of pads satisfy this requirement better for a tracks emerging from a centred interaction vertex; this geometry was chosen in the design of the ALEPH TPC.

10.5 Choice of the gas filling

The choice of the gas for operating a TPC has to satisfy often conflicting requirements, depending on the detector's application and desired performances. For large volume devices it is convenient, if not mandatory, to select an operating point

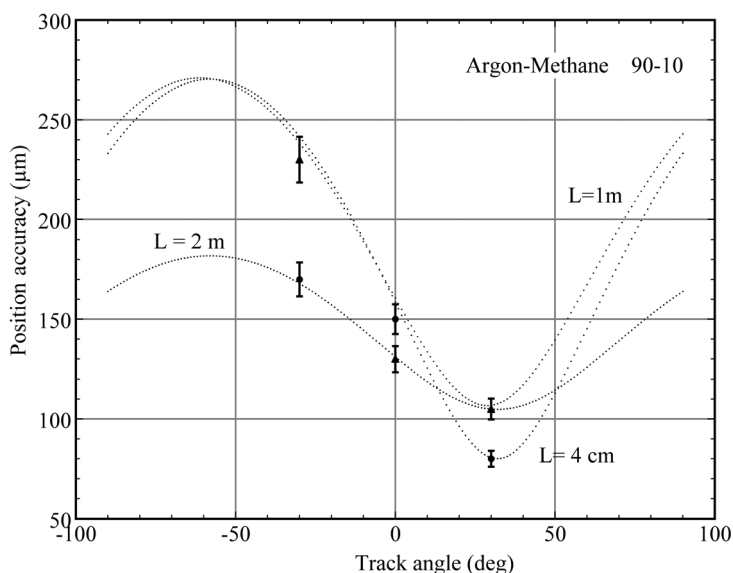


Figure 10.29 Position accuracy as a function of track angle for several drift lengths. Points with error bars are measurements from the ALEPH TPC. (Sharma, 1996). By kind permission of A. Sharma.

requiring moderate electric fields to avoid too high values of voltage on the cathodes. In many mixtures this results in low, non-saturated drift velocities and large electron diffusions, affecting the rate capability and localization accuracy of the detector. As shown in Figure 10.30, a standard argon–methane 90–10 mixture (P10) satisfies the requirements of a high drift velocity and low diffusion at moderate drift field values, and has been the preferred choice for the first generation of TPCs, with a peaking drift velocity around 150 V/cm and a strong reduction of the traverse diffusion at high magnetic fields.

Requiring increasingly stringent safety measures because of their flammability, the use of hydrocarbon-rich gases has become less and less popular. A replacement of methane with carbon dioxide, although satisfying the diffusion requirements despite a lower drift velocity, is discouraged due to the instabilities and secondary processes observed in the MWPC operation. Safer mixtures with reduced methane content have been studied in the framework of the International Linear Collider detector with the so-called TDR¹ gas; reaching a saturated mode of operation requires fields larger than for P10, as seen in Figure 10.31; the transverse diffusion suppression is, however, comparable (Behnke *et al.*, 2001).

For detectors operating without a magnetic field, and if one of the major requirements is a good two-track resolution, neon–carbon dioxide mixtures are

¹ ILC Technical Design Report.

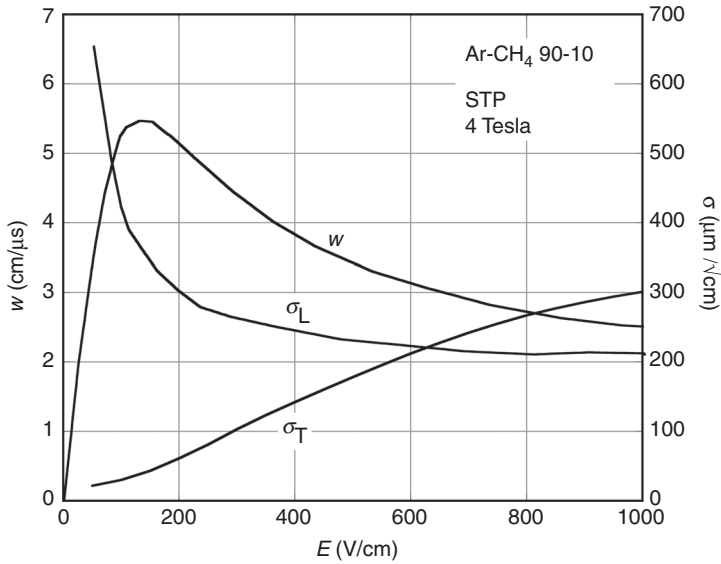


Figure 10.30 Electron drift velocity, longitudinal and transverse diffusion coefficient in 4 T in argon–methane 90–10.

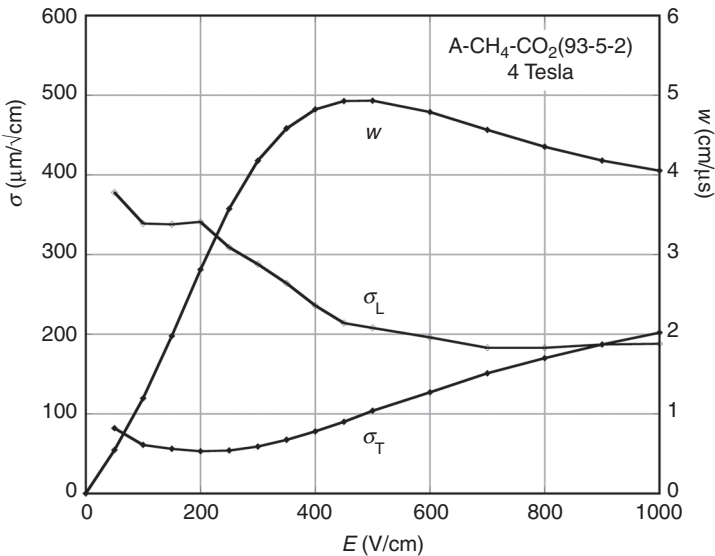


Figure 10.31 Electron drift velocity, longitudinal and transverse diffusion coefficient in 4 T in argon–methane–carbon dioxide.

preferred; in Figure 10.32, measured values of the charge distribution on reaching the anodes after 60 cm drift in the transverse (a) and drift direction (b) are compared (Afanasiev *et al.*, 1999). The neon–CO₂ mixture has been chosen for the vertex TPCs in the NA49 experiment (Fuchs, 1995).

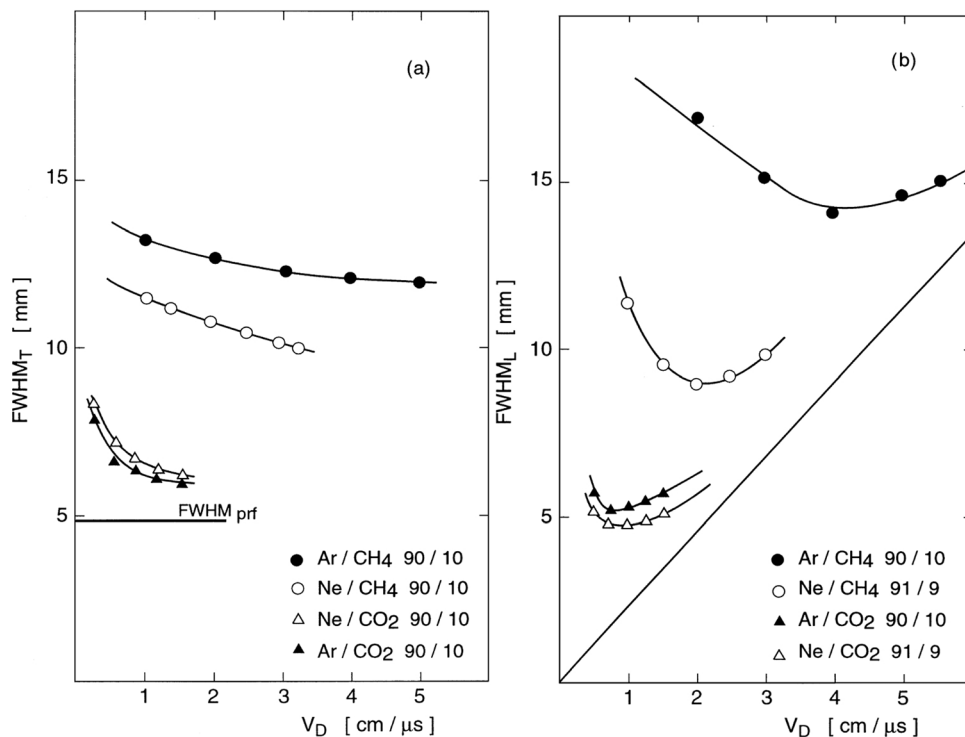


Figure 10.32 Transverse (a) and longitudinal width (b) of the charge distribution after 60 cm drift in several gas mixtures (Afanasiev *et al.*, 1999). By kind permission of Elsevier.

Pure carbon tetrafluoride (CF_4) has intrinsically many desirable properties: the highest known drift velocity, favouring its use in fast detectors, a very low transverse diffusion, even in absence of a magnetic field (Figure 10.33), and reduced sensitivity to thermal neutron background as compared to hydrogenated molecules; these advantages are balanced by the need to apply very high voltages to achieve charge multiplication. Promising results obtained with a prototype TPC with MWPC readout have been reported (Isobe *et al.*, 2006). Coupled to gas electron multiplier sensors, CF_4 -filled TPCs have been demonstrated to provide excellent space resolutions (Oda *et al.*, 2006), see Chapter 13.

10.6 Coordinate in the drift direction and multi-track resolution

As already mentioned, most TPCs have been optimized for the measurement of the projected azimuthal coordinate, in the plane of the wires and pad rows; the readout electronic, designed to record the charge distribution of induced signals on pads with good amplitude resolution, usually has a modest time resolution, corresponding to the separation between successive time slices.

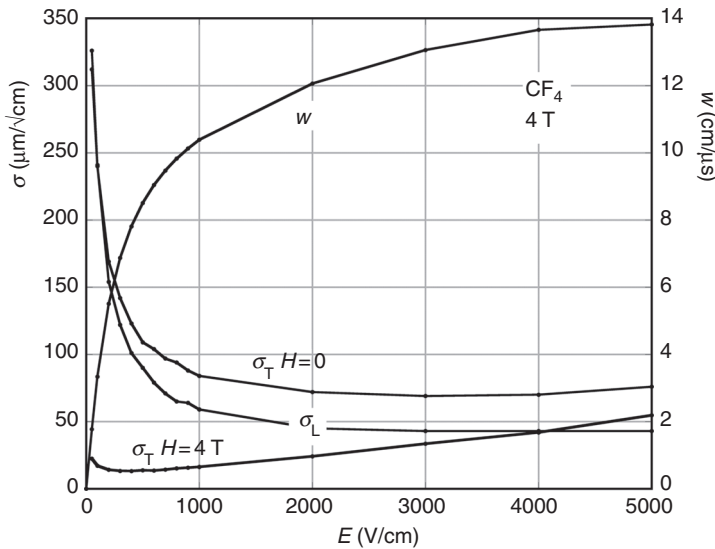


Figure 10.33 Drift velocity and diffusion coefficients in pure carbon tetrafluoride at NTP.

When tracks are sampled over many time slices, a fitting algorithm can provide a better estimate of the drift coordinate, only limited by the dispersions due to diffusion. It should be remembered that the longitudinal diffusion coefficient is not reduced by magnetic field, so even using a fast time recording system on the anode wires, the drift time measurement provides a modest resolution for long detectors. All considerations discussed in Chapter 9 apply for this case. Figure 10.34 is an example of longitudinal space resolution as a function of drift length, measured with the ALICE TPC for increasing values of the angle between the tracks and the normal to the anode wires (Alme *et al.*, 2010).

The multi-track separation is limited in the projection plane by the width of the pad response, and in the longitudinal direction by the time width of the signals, and is therefore geometry and electronics dependent. As an example, Figure 10.35 shows the two-track resolution measured with the STAR TPC (Anderson *et al.*, 2003).

Essential for ensuring the required extreme multi-track capability of the detector is the use of custom-made fast amplifier-ADC ASIC, performing on-board, digital pedestal correction and zero-suppression; Figure 10.36 is an example of detected signal for a high-multiplicity event, before and after the digital shaping performed by the circuit (Mota *et al.*, 2004).

A detailed study of signal shape in TPCs for various geometry and operating conditions, aiming at improving the multi-track resolution, is given in Rossegger and Riegler (2010).

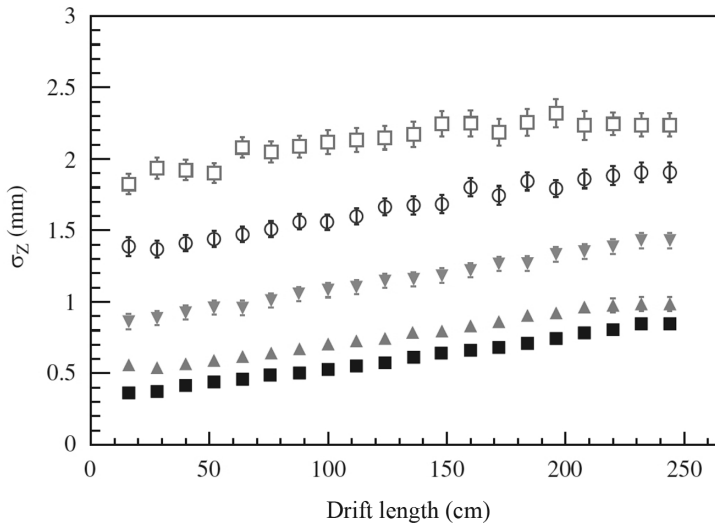


Figure 10.34 Longitudinal resolution as a function of drift length. Sets of points corresponds to $\tan(\alpha) = 0$ (lowest values) up to $\tan(\alpha) = 0.92$ in steps of 0.23, where α is the angle between the tracks and the perpendicular to the anodes (Alme *et al.*, 2010). By kind permission of Elsevier.

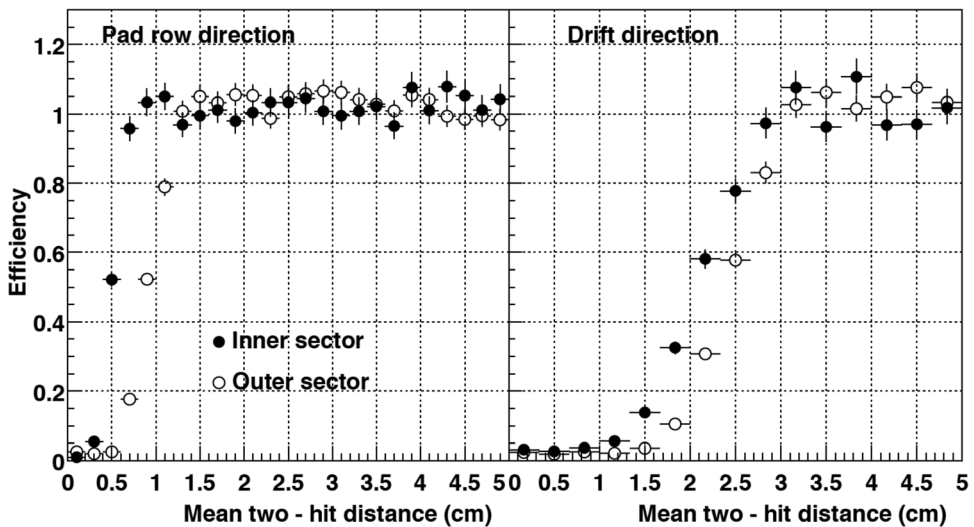


Figure 10.35 Two-track resolution in the pad and drift directions measured with the STAR TPC (Anderson *et al.*, 2003). By kind permission of Elsevier.

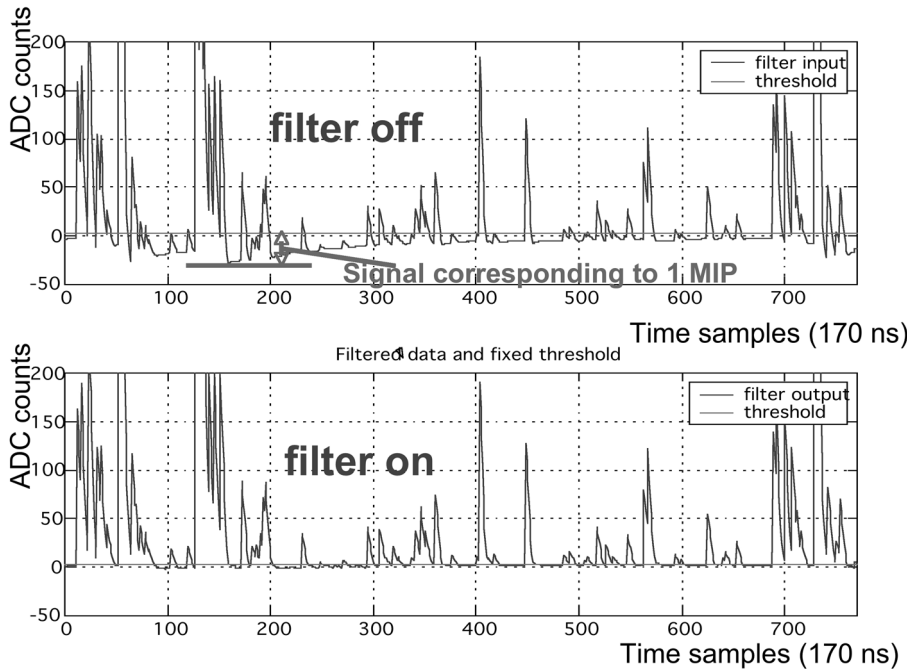


Figure 10.36 Digital filtering of a pad signal to improve multi-track resolution (Mota *et al.*, 2004). By kind permission of Elsevier.

10.7 Positive ion backflow and gating

The effects on charge multiplication of the positive ions produced in the avalanches were discussed in Chapter 8. In large volume drift chambers, TPCs in particular, a fraction of these ions recede into the drift volume and accumulate with a density that depends on the production rate and the total drift time, typically several hundred ms per metre of drift. For even modest counting rates, the ensuing electric field modification introduces distortions in the drift path, largely exceeding the desired localization accuracy. Although in principle these distortions can be estimated from the knowledge of the physical track density distribution, correcting the effect is rather complex.

It should be noted that, at the moderate proportional gains, around 10^4 , normally used to limit the ions production rate, and as discussed in Section 8.9, the avalanches develop preferentially on the drift side of the anode, with the consequence that the majority of ions recede in the direction of the incoming tracks; they then transfer into the drift volume in a percentage corresponding to the ratio between the drift and the MWPC gap fields, typically 10–20% of the total.

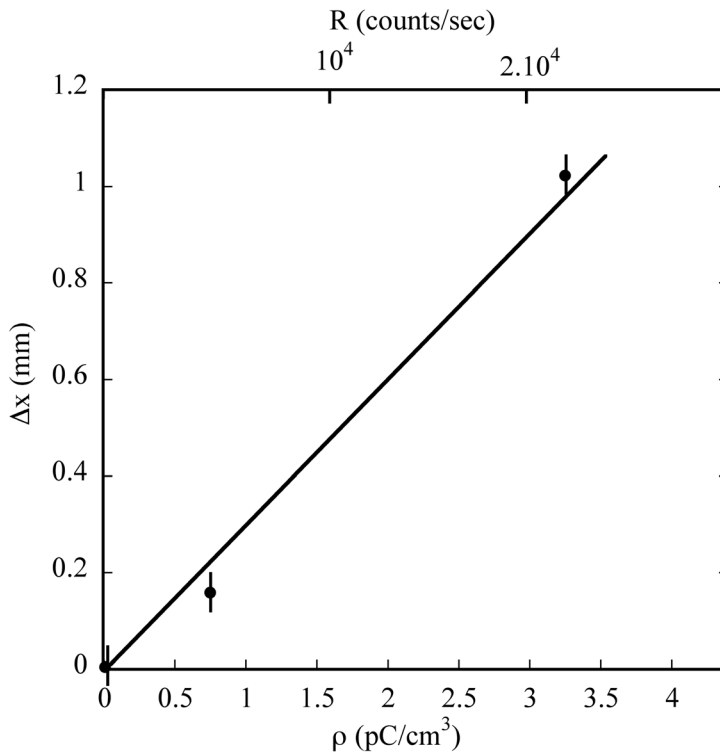


Figure 10.37 Lateral displacement of the recorded position of a collimated ^{55}Fe source after 10 cm of drift close to the positive charge cloud produced by a strong source, 10 mm apart, with the intensity given in the top scale (Friedrich *et al.*, 1979).

For a radiation flux releasing R electrons per second, the positive ions density is given by (Friedrich *et al.*, 1979):

$$\rho^+ = \frac{e R L \varepsilon M}{w^+},$$

where w^+ and L are respectively the ion's drift velocity and drift length, M is the proportional gain and ε is the fractional ion feedback. The ensuing field modification can be computed using standard electrostatic methods; for a uniform space charge distribution in the drift volume, the field strength is decreased in the region close to the end-cap and increased towards the drift electrode. Although in this case the electron drift lines are not changed, the variation of field results in a non-constant drift velocity.²

² The integral of the field over the gap has of course to remain constant and equal to the difference of potential divided by the gap.

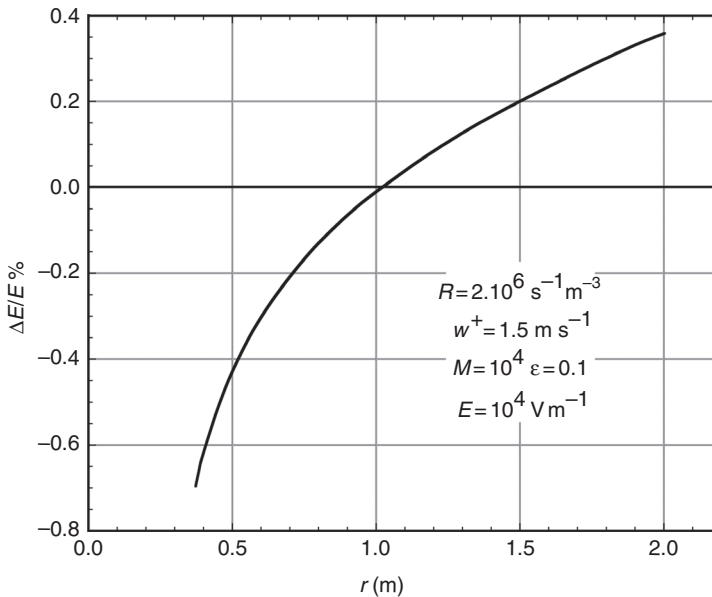


Figure 10.38 Percentage drift field modification as a function of radius, computed in the ALEPH TPC operating conditions shown in the inset.

In the case of a non-uniformly distributed charge accumulation, the field is also modified in direction; electrons drifting near a column of positive charge are attracted inwards. Measured with a small TPC-like drift chamber, Figure 10.37 shows the lateral displacement of the recorded position after 10 cm of drift of a collimated source, 1 cm away from the positive charge sheet produced by a second source with the rate indicated on the upper scale (Friedrich *et al.*, 1979).

For a cylindrical TPC with inner and outer radii r_1 , r_2 , and assuming a uniform charge density $\rho^+(r) = \rho_0$, the radial perturbation of the field is (Blum and Rolandi, 1993):

$$E(r) = \frac{\rho_0}{2 \varepsilon_0} \left(r - \frac{r_2^2 - r_1^2}{2r \ln(r_2/r_1)} \right).$$

Figure 10.38, computed from the expression above, shows the percentage field modification as a function of radius for the standard operating conditions of the ALEPH TPC, as given in the inset.

An effective way to substantially reduce the ion feedback is to insert between the MWPC cathode and the drift volume a wire mesh, or gating grid, opened or closed to the charge flow under control of an external voltage. While a simple mesh at an appropriate potential cancelling the drift field would be effective, a grid of parallel field wires, alternately connected to positive and negative voltages, is a more convenient geometry, minimizing the transient's pickup on signal electrodes

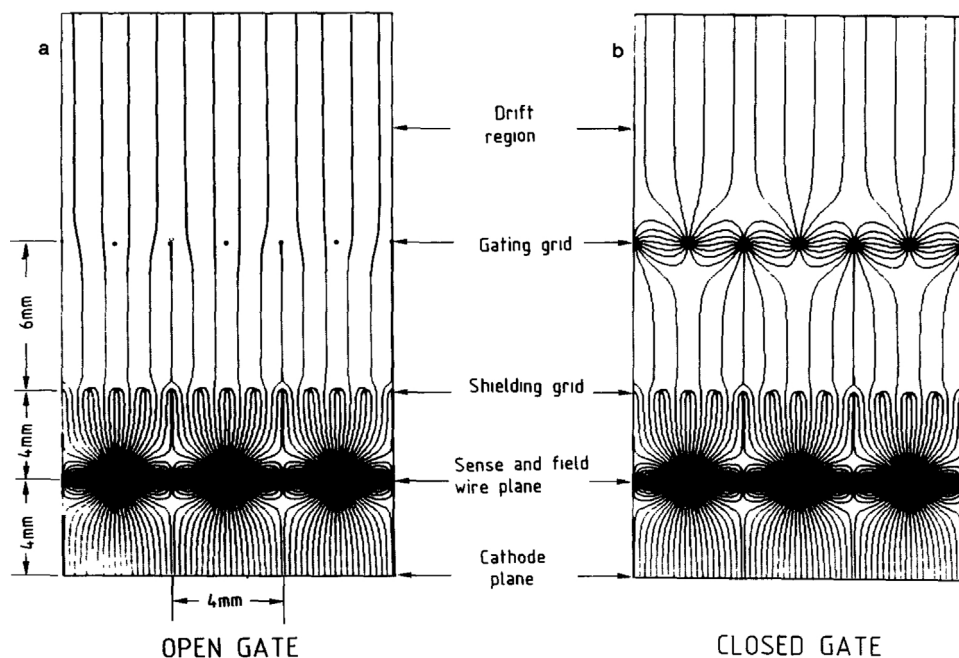


Figure 10.39 Principle of operation of the gating grid; open to the drifting charges when wires are kept at the same potential, the grid is closed with the application of a voltage difference to alternate wires (Amendolia *et al.*, 1985a).

at the time of application of the gating pulse. In the open gate mode, the grid wires are connected to the same voltage V_G , corresponding to the local drift field equipotential; to close the gate, a symmetric bipolar field $\pm\Delta V_G$ is added to alternate wires, as shown schematically in Figure 10.39 (Amendolia *et al.*, 1985a).

The gating grid can be operated in two modes: always open and closed to the ions' backflow on detection of an event, or always closed and open to ionization electrons in coincidence with a trigger and for a time equal to the total drift time. In the second case, due to the time taken to generate and distribute the transparency restoring voltage pulses, a layer of drift a few cm thick close to the end-cap is lost to detection. In either mode, the goal is to reach an ion suppression factor equal to or better than the detector gain.³

Aside from small losses due to the different diffusion coefficient, an electrical gate open to electrons in one direction transmits all ions in the opposite one. This is not the case in the presence of a magnetic field, due to the different drift line modification due to the Lorentz force affecting only electrons; for a proper choice of the polarization of the gating grid, all ions are stopped, independently of the value

³ Based upon the consideration that at this value the ions' feedback equals the unavoidable contribution of primary ionization.

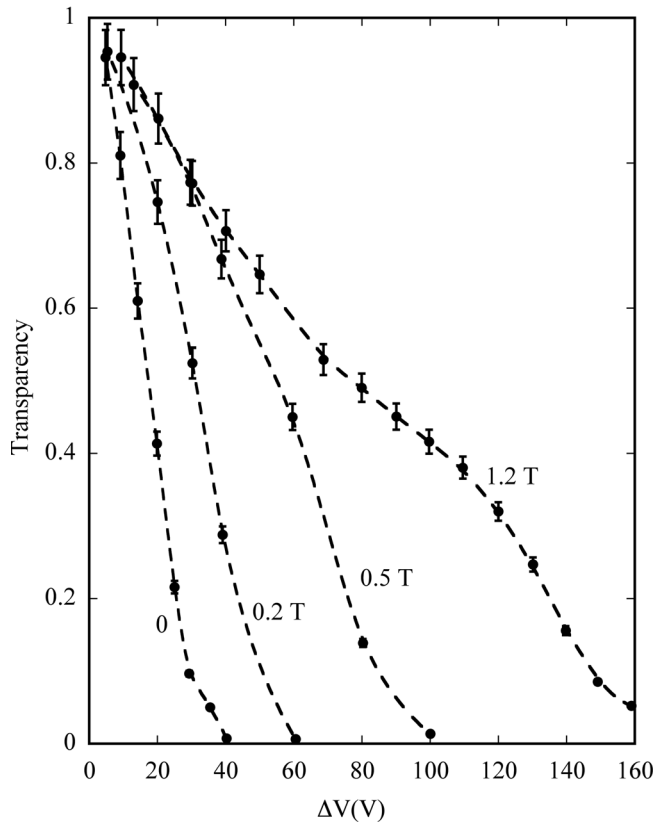


Figure 10.40 Electron transparency of a gating grid as a function of polarization voltage, for increasing values of the magnetic field (Amendolia *et al.*, 1985b).

of the magnetic field, while the electron transparency is partly restored at high field values, as shown in Figure 10.40 (Amendolia *et al.*, 1985b). While very attractive since not requiring the application of pulsed potentials, the ‘ion diode’ has not often been used because of the large distortions introduced due to the $E \times B$ effect.

The problem of the reduction of the positive ions’ backflow has been analysed in great detail during the development of the new generation of TPCs with micro-pattern gas detector readout, covered in Chapter 13.

Gating is a very effective way to reduce or eliminate the field distortions generated by the accumulation of positive ions in the drift volume; however, it can only be used for relatively small event rates, with the average distance between events comparable with the maximum electron drift time, as for the LEP detectors. When gating is not possible, operation of the detector at a smaller proportional gain and an optimization of geometry aiming at reducing the ions’ backflow, coupled with suitable analytical calculations to estimate the space charge distribution, may allow one to correct the distortions (Rossegger *et al.*, 2010; Rossegger *et al.*, 2011).

The new generation of micro-pattern devices, aside from providing an improved track resolution, permit a strong reduction of the positive ions' backflow when used as end-cap TPC detectors.

10.8 TPC calibration

While a maximum effort is put into the design and construction of large TPCs to keep strict tolerances on all sources of distortion that can affect the final performance, a thorough monitoring of operating and ambient parameters is needed, together with an extensive calibration procedure. The proportional gain can be monitored with the use of external radioactive sources; placed in known positions on the drift electrode, they permit the control of gain and/or capture losses as well as the presence of distortions of the electrons drift lines.

A very powerful tool to perform tracking calibrations is the use of pulsed laser beams ionizing the TPC gas and emulating straight tracks at strategic positions and angles; advantages of using laser-generated tracks are the favourable ionization statistics (Poisson-like, without long-range δ electrons), controlled ionization density and insensitivity to magnetic field.

Pulsed nitrogen and frequency-doubled Nd:YAG lasers, emitting at 337 nm (3.68 eV) and 226 nm (4.68 eV) respectively, are commonly used, with sub-ns timing resolutions; two-stage N₂ lasers have been developed, offering very high intensity and low divergence beams.

For the gases normally used in detectors, ionization requires two- or three-photon excitation and therefore high power density. The ionization density can be largely increased by adding a controlled amount of a low ionization potential vapour in the gas mixture; the presence of pollutants is often sufficient by itself to enhance the ionization rate. Many compounds have been tested; for a review see for example Hilke (1986a). However, in view of the severe ageing problems that have been encountered by the voluntary or unwanted addition of trace organic compounds, the use of additives should be considered with care (see Chapter 16) and in general the solution requiring higher power density has been preferred, although it is often recognized that a good fraction of the ionization is produced by the presence of unknown impurities; the laser power is adjusted to obtain the desired ionization density.

Various methods have been implemented to generate multiple laser tracks covering the sensitive volume, with one or more high-power lasers and arrangements of fixed beam splitters and mirrors, as used for ALEPH (Decamp *et al.*, 1990), DELPHI (Brand *et al.*, 1989) and ALICE (Alme *et al.*, 2010), or systems of remotely controlled rotating mirrors (Miśkowiec and Braun-Munzinger, 2008).

The straight track reconstruction permits one to correct for mechanical tolerances, drift path distortions, temperature and gas variations; the large ionization yield resulting from a laser beam hitting the cathode can be used for continuous drift velocity monitoring.

10.9 Liquid noble gas TPC

Very powerful in the detection and tracking of complex events, standard TPCs are unsuitable in the search for rare events such as neutrino interactions, proton decays and other exotic particles for which a gas has a very low cross section. Proposed in the seventies by Carlo Rubbia and collaborators, the liquid argon TPC has a density several orders of magnitude larger, and a correspondingly higher interaction probability.

While observed in liquid noble gases, charge multiplication is hard to exploit as it requires the use of very thin anode wires (Derenzo *et al.*, 1974). The devices operate in the ionization mode, collecting the electrons released in the sensitive volume; the higher ionization density of the charged prongs compensate for the lack of gain. The charge is collected and detected on two perpendicular wire grids at a close distance; in some designs, a screening grid separates the sensitive volume from the sensors electrostatically. Proper choice of the electric field strength ensures that most of the electrons pass the screening and the first induction grid before being collected by the last mesh.

To avoid electron losses by capture, paramount for the operation of the LAr-TPC is the degree of purity of the liquid. A substantial effort has been devoted to the identification and removal of sources of electro-negative pollutants, increasing the electron lifetime to several ms, well above the maximum drift time of large detectors (Buckley *et al.*, 1989; Bettini *et al.*, 1991).

In the framework of the ICARUS experiment, implemented in the underground Italian Gran Sasso National Laboratory (LNGS), increasingly large LAr-TPC prototypes have been built and operated, demonstrating lossless charged particle tracking up to 140 cm of drift length (Arneodo *et al.*, 2000). Commissioned in 2004, the ICARUS T600 detector has 500 tons of sensitive volume (Amerio *et al.*, 2004); its modular conception permits to increase the volume further. Figure 10.41 is an example of a cosmic ray shower detected with the device and demonstrates its multi-track resolution.

Simultaneous detection of the argon scintillation with photomultipliers can be exploited to provide the time of the event, and serve as trigger for the data acquisition (Cennini *et al.*, 1999).

Other developments of cryogenic and dual-phase detectors are described in Section 15.2.

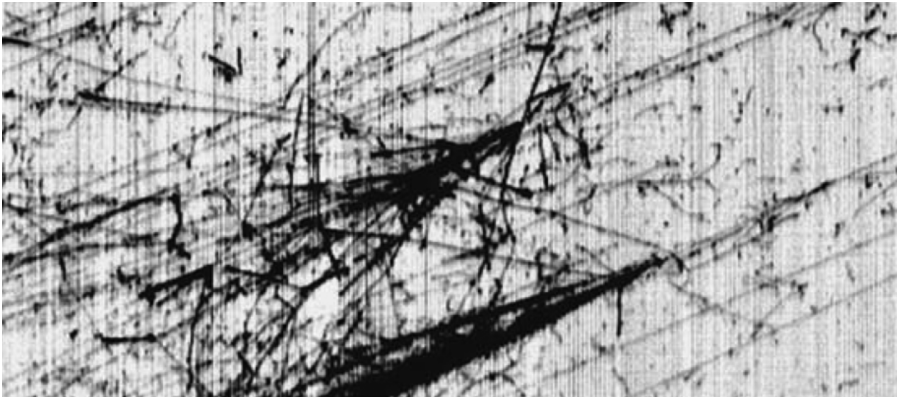


Figure 10.41 Cosmic ray shower recorded with the ICARUS T600 LAr-TPC (Amerio *et al.*, 2004).

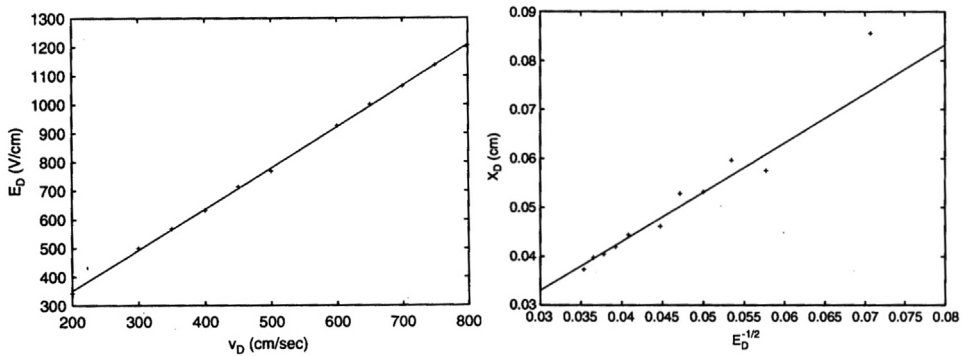


Figure 10.42 Drift velocity (left) and longitudinal diffusion (right) for an 80 cm drift for CS_2^- ions as a function of electric field (Martoff *et al.*, 2005).

10.10 Negative ion TPC

As discussed in the previous sections, the space resolution of drift chambers, and of TPCs in particular, is limited by the diffusion of electrons during their drift. While the transverse diffusion is reduced by a strong magnetic field parallel to the electric field, the longitudinal diffusion, determining the localization accuracy in the drift direction, is not affected. It has been proposed (Martoff *et al.*, 2000) to exploit the electron capture properties of some molecules to transform the drifting species from electrons to negative ions, having intrinsically much smaller diffusion (see Chapter 4). Detection relies on the observation that on arrival in the high field of the multiplying end, negative ions can be stripped of their captured electron and give origin to a charge-amplifying avalanche.

The drift properties of negative ions have been investigated with a small TPC with pure carbon disulfide and Ar-CS₂ gas fillings, both at low and atmospheric pressures (Ohnuki *et al.*, 2001; Martoff *et al.*, 2005). Electrons are extracted from the drift electrode by an intense flash of UV light and quickly captured by the electro-negative gas to form negative ions; the arrival time and shape of the delayed pulse at the anodes are analysed to deduce the drift velocity and longitudinal diffusion coefficient. Results of the measurements of drift velocity and longitudinal diffusion for an 8 cm drift in a He-CS₂ mixture are shown in Figure 10.42 (Martoff *et al.*, 2005); values are consistent with the expectation for ions.

Potentially interesting to achieve very good space resolutions, a negative ion chamber has a major drawback in the very long drift time, limiting its use to the detection of rare events as, for example, in dark matter and WIMPs research (Alner *et al.*, 2004).